



Cite this: *RSC Adv.*, 2022, **12**, 16491

Received 5th May 2022
 Accepted 27th May 2022

DOI: 10.1039/d2ra02844a
rsc.li/rsc-advances

Introduction

Natural products have always been the inspiration for the development of drugs and probes.¹ In addition to their biological activity, structural determination, and total synthesis, it is above all the knowledge of their molecular targets and mechanism of action that is of central interest in current natural product research.² Analysis of the clinical trials suggests that the late stage failures of candidate drug molecules in phase II or III clinical trials are frequently caused by off-target effects or inefficient target engagement *in vivo*. And major factors contributing to failures are insufficient proof of target engagement.³

Necrosis, one mode of cell death, is a hallmark for severe diseases in many pathologies, such as cancers, cardiovascular disorders, neurodegeneration and also in the way malignant tumors respond to cancer therapy.^{4,5} As a result, noninvasive techniques for necrosis detection can be used to accomplish several goals including supporting disease diagnosis, assessing the extent of tissue damage and evaluating cancer therapeutic efficacy. But these noninvasive techniques are lacking in the clinic, only radiolabeled annexin V⁶ and [¹⁸F]ICMT-11 in clinical trials.⁷ Our group demonstrated that a certain class of

natural necrosis avid agents like hypericin and rhein, which can specifically accumulate in the necrotic area of diseases (Fig. 1).⁸⁻¹⁴ Moreover, in order to understand the necrosis avidity mechanism of rhein derivatives, we had explored the cellular localisation of rhein by synthesising a clickable derivative and labelling it *in situ* with an Alexa-fluor 488 click partner mediated by copper (CuAAC) in bioorthogonal click chemistry, that indicates the colocalization between rhein and nucleus including nucleoli.¹⁵ However, more recent studies show that the toxicity of Cu(i) has limited the use of this particular reaction for *in vivo* applications, and CuAAC also denatures and causes protein aggregation and precipitation, which may make it incompatible with some downstream applications.¹⁶ Moreover, the copper-based CuAAC methodologies in fixed cells implicated Cu(i)/alkyne intermediates in the non-specific localisation of ligands to the nucleoli.¹⁷ Therefore, our research on the necrosis targeting mechanism of rhein needs to be further proofed. Hence, we developed a strategy that allows identification of target occupancy measurement of rhein derivatives under physiological conditions, using bioorthogonal copper-free click chemistry in live cells (Fig. 2).

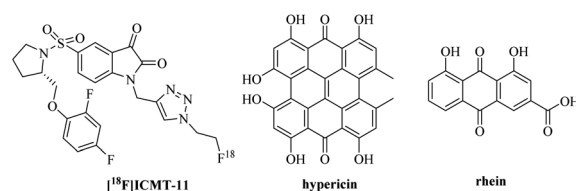


Fig. 1 Chemical structure of [¹⁸F]ICMT-11, hypericin and rhein.

^aAffiliated Hospital of Integrated Traditional Chinese and Western Medicine, Nanjing University of Chinese Medicine, Nanjing 210028, Jiangsu, China. E-mail: jqmxy@163.com

^bLaboratories of Translational Medicine, Jiangsu Province Academy of Traditional Chinese Medicine, Nanjing 210028, Jiangsu, China

† Electronic supplementary information (ESI) available: Experimental procedures and spectroscopic data. See <https://doi.org/10.1039/d2ra02844a>.

‡ These authors contributed equally to this work.



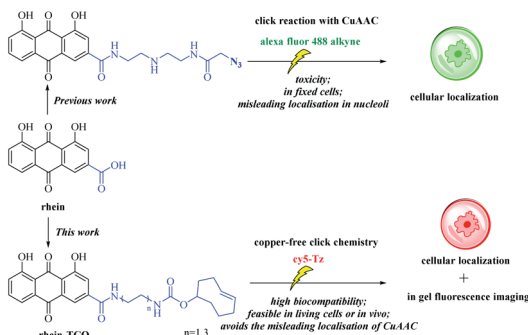


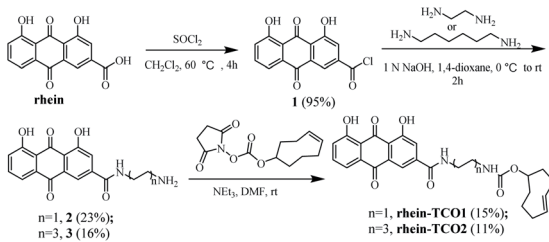
Fig. 2 A new functionalized rhein probe containing a bioorthogonal moiety (copper-free click-probe) usable for assay in live cells.

Results and discussion

Based on previous structure–activity relationship, the rhein was equipped with a spacer bearing a terminal azide function, grafted onto position 3 of the anthraquinone core, so as to have a minimal effect on its necrotic affinity. We therefore designed and synthesized compound **rhein-TCO1** and **rhein-TCO2**, which both contain the bioorthogonal moieties either *trans*-cyclooctene (TCO) (Fig. 2).

The preparation of **rhein-TCO1** and **rhein-TCO2** is outlined in Scheme 1. The synthesis used the commercially available rhein as starting material. Rhein reacted with thionyl chloride to furnish an intermediate acyl chloride **1**, which then coupled with ethylenediamine or 1,6-hexamethylenediamine to form amide **2** or **3** under basic conditions. Subsequently, amide **2** or **3** was reacted with (*E*)-cylooct-4-en-1-yl (2,5-dioxopyrrolidin-1-yl) carbonate to yield target compound **rhein-TCO1** and **rhein-TCO2**. The structure of **rhein-TCO1** and **rhein-TCO2** was established by analysis of their NMR data (ESI[†]) and mass spectrometry.

First, in order to investigate whether the modified **rhein-TCO1** and **rhein-TCO2** maintain the same necrotic targets as rhein, the necrosis avidities of rhein, **rhein-TCO1** and **rhein-TCO2** were evaluated *in vitro* and *in vivo* by labeling with radioisotope iodine-131, which has been proved as feasible and convenient method with high detective sensitivity.¹⁸ The iodogen coating method was conducted successfully in this study.¹¹ A radiochemical purity greater than 98% (labeling yield more than 90%) could be obtained as measured by analytical RP-HPLC for all tracers. The labeled compounds turned out to



Scheme 1 Synthetic routes for **rhein-TCO1** and **rhein-TCO2**.

be stable after incubation in rat plasma at 37 °C for 24 h the data of 93.11% ± 0.47% (rhein), 96.07% ± 0.52% (**rhein-TCO1**) and 95.01% ± 0.38% (**rhein-TCO2**). Then, the necrosis affinities of rhein, **rhein-TCO1** and **rhein-TCO2** were assessed by determining the uptakes of ¹³¹I-rhein, ¹³¹I-**rhein-TCO1** and ¹³¹I-**rhein-TCO2** in necrotic A549 cells and normal A549 cells *in vitro*. Necrotic A549 cells were induced under intense hyperthermia at 57 °C for 1 h according to previous reports and the percentage of necrotic cells were in the range of 75–85% as determined by flow cytometry. As shown in Fig. 3 and Table S1,[†] the necrotic-to-viable uptake ratios of ¹³¹I-rhein, ¹³¹I-**rhein-TCO1**, ¹³¹I-**rhein-TCO2** and ¹³¹I-**rhein-TCO2** under rhein blocking were 3.14, 2.14, 3.08 and 1.41, respectively. ¹³¹I-**rhein-TCO2** features significant necrotic affinity *in vitro* as ¹³¹I-rhein. The ratios were considerable compared with other previously explored NAAs (2.50–2.80).¹⁹ Disappointingly, ¹³¹I-**rhein-TCO1** with 2C alkyl chain spacer, which might hinder the binding of rhein to the target, showed lower necrotic affinity. Moreover, the significantly decreased uptake ratios *in vitro* rhein blocking experiment indicated that ¹³¹I-**rhein-TCO2** and rhein should share the same specific target of necrotic cells.

To investigate the necrosis targeting ability of **rhein-TCO1** *in vivo*, biodistribution study was performed for accurate quantification of the tracer uptake in the selected organs in mice with muscular necrosis by gamma counting (p.i.) (Fig. 4 and Table S2[†]). As showed in Fig. 4, significantly higher and specific radioactivity uptakes of both compounds in necrotic muscle compared to normal muscle ($P < 0.05$). The concentrations of ¹³¹I-rhein in necrotic *vs.* normal muscle were $2.29 \pm 0.51\% \text{ ID/g}$ *vs.* $0.42 \pm 0.11\% \text{ ID/g}$ with the corresponding radioactivity ratios from necrotic to normal muscle were 5.49. And the necrotic-to-normal muscle ratios were 5.38 for ¹³¹I-**rhein-TCO2**. The organ that stand out was the excretion organ bladder. Other organs or tissues like kidneys, stomach, blood also showed high uptakes of ¹³¹I-rhein and ¹³¹I-**rhein-TCO2**. These prominent radioactivities revealed that both compounds showed high and specific necrosis affinity in necrotic organs or tissues and were mainly metabolized and/or excreted by a renal pathway. The average radioactivity uptakes of ¹³¹I-**rhein-TCO2** were slightly lower than that of ¹³¹I-rhein in almost all organs and tissues, which would

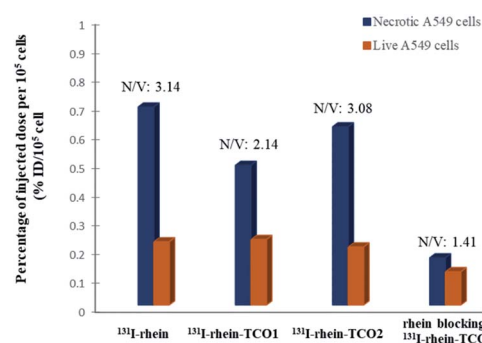


Fig. 3 *In vitro* necrotic cell uptakes of compound ¹³¹I-rhein, ¹³¹I-**rhein-TCO1**, ¹³¹I-**rhein-TCO2** and rhein blocking. Data were displayed as average percentage uptake per 10^5 cells plus or minus standard deviation (% uptake per 10^5 cells). N/V: ratio of necrotic/live A549 cells.



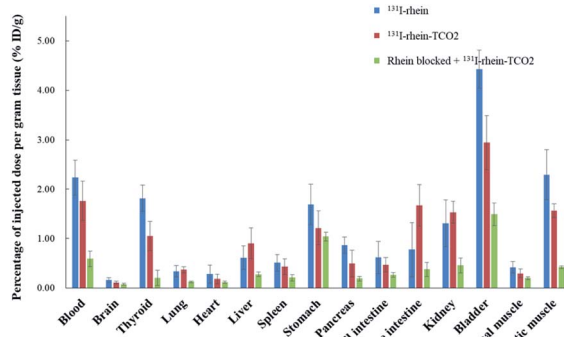


Fig. 4 Biodistribution of ¹³¹I-rhein, ¹³¹I-rhein-TCO2 in unblocked and 10 mg kg⁻¹ rhein blocked (rhein blocked + ¹³¹I-rhein-TCO2) in mice models of muscular necrosis at 6 h ($n = 5$ /group) by gamma counting (p.i.). Data were displayed as average percentage injected dose per gram of tissue plus or minus standard deviation (% ID/g \pm SD).

be consistent with the results obtained by uptakes in necrotic A549 cells. The reason might be that the prolongation of the linker increased the lipophilicity of the tracer, which had a slightly effect on its uptakes in cells and *in vivo* distribution properties. Furthermore, the blocking experiment, which was a strategy for target identification of **rhein-TCO2** by competitive binding with rhein, was devised to demonstrate that **rhein-TCO2** shares the same target *in vivo* as rhein. In good agreement with rhein-based competitive binding *in vitro* experiments, the excessive unlabeled rhein significantly reduced the uptake of ¹³¹I-rhein-TCO2 in necrotic muscle compared with the unblocked group. The results were also confirmed by autoradiography and H&E staining in Fig. 5. These data confirm that, in necrotic tissues, **rhein-TCO2** and rhein should share the same specific targets.

We next assessed the clickable compound **rhein-TCO2** in necrotic A549 cells by confocal fluorescence microscopy imaging (Fig. 6). A negative control experiment was performed without **rhein-TCO2**. And confocal fluorescence microscopy

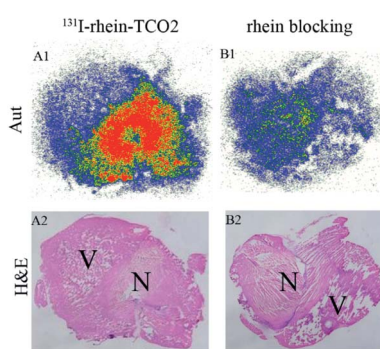


Fig. 5 Autoradiograms (Aut) (upper panels), corresponding H&E staining images (under panels) of ¹³¹I-rhein-TCO2 and ¹³¹I-rhein-TCO2 with 10 mg kg⁻¹ rhein blocked from mice model of muscular necrosis at 6 h after injection. (A1 and A2) ¹³¹I-rhein-TCO2, (B1 and B2) ¹³¹I-rhein-TCO2 with 10 mg kg⁻¹ rhein blocked, respectively. N = necrotic area; V = viable area.

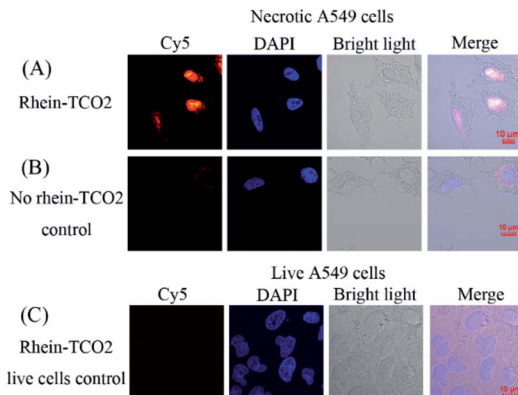


Fig. 6 Confocal imaging of necrotic and live A549 cancer cells co-stained with DAPI (blue). Cy5 (red), DAPI (blue), corresponding bright field and the merged images are shown. (A) Necrotic A549 cells treated with **rhein-TCO2** (50 μ M, 3 h) and subsequent reacted with Cy5-Tz for 30 min; (B) necrotic A549 cells treated without **rhein-TCO2** and only with Cy5-Tz for 30 min; (C) live A549 cells treated with **rhein-TCO2** (50 μ M, 3 h) and then reacted with Cy5-Tz for 30 min. Scale bar = 10 μ M.

studies were also conducted on live A549 cells to confirm the specific uptake of compound **rhein-TCO2** on necrotic cells (Fig. 6B and C). Fig. 6A shows that the distribution of red fluorescence (Cy5) was basically consistent with that of blue fluorescence through the location of DAPI stained nucleus and the morphology of A549 cell observed under white light, and it could be inferred that **rhein-TCO2** was mainly distributed in the nucleus (red fluorescence). We observed the same results in other fields of parallel experiments (Fig. S1†). As seen in Fig. 6 and S1A,† the nuclear marker DAPI could dye the entire shape of the nucleus and did not stain the nucleolar subcompartments, which appeared as dark areas at the same time. This is likely due to the fact that DAPI mainly performs nuclear staining by binding with DNA, and its binding ability with RNA is much weaker than that of DNA. Nucleoli are highly dense domains characterised by the strong spatial confinement of nucleic acids (mainly rRNA, very small amounts of DNA) and proteins, so the blue fluorescence of DAPI can hardly be observed in nucleoli.²⁰ However, it is worth noting that red fluorescent signal of Cy5 located **rhein-TCO2** was observed throughout the whole nucleus without nucleolar cavity, and the fluorescence intensity was even greater in the nucleolar region. These results indicated that **rhein-TCO2** can be distributed throughout the nucleus. Similar results were obtained when the compound with 2C alkyl chain spacer (**rhein-TCO1**) was examined (see Fig. S1B†). But in this case, red fluorescence could also be observed in the cytoplasm, indicating that the targeting ability of **rhein-TCO1** to the necrotic nucleus was weaker than **rhein-TCO2**. And this result was also consistent with the previous results of the necrotic targeting ability. Next, we investigated the interference of Cy5-Tz dye. Necrotic A549 cells were incubated with Cy5-Tz for 30 min without **rhein-TCO2**. There was almost no red fluorescence in the entire cell can be observed when no **rhein-TCO2** was introduced (Fig. 6B). In



contrast to the results in Fig. 6A, the cytoplasm of one of the cells showed weak red fluorescence, but by superposition comparison with DAPI, it could be seen that the nucleus presented a Cy5-Tz free (red fluorescence) void state, and thus most likely speculated that the red fluorescence in the nucleus was derived from the specific nuclear distribution of **rhein-TCO2**, excluding the interference of Cy5-Tz dye. Moreover, the same post labelling strategy was applied in the localization of **rhein-TCO2** in live A549 cells. And not surprisingly, no significant staining and/or localization was observed, which proved the specific uptake of **rhein-TCO2** on necrotic cells (Fig. 6C).

Up till now, the universal targets for developing molecular probes that can be used for visualization of necrotic cell include intracellular DNA, Hsp90 (90 kDa heat shock protein), fumurate, La antigen, histones and some unknown constituents.^{21,22} The conclusion to be drawn from the confocal experiments is that **rhein-TCO2** is mainly distributed in the nucleus of necrotic cells. In addition, rhein is a primary anthraquinone, which has a planar structure and is likely to achieve necrosis targeting by binding to DNA. Then, we designed DNA electrophoresis experiments based on biological orthogonal reaction in a randomly linearized plasmid pUC19 DNA to further verify whether **rhein-TCO2** can bind to DNA. The procedure involved incubation of the pUC19 DNA with **rhein-TCO2** and reaction with Cy5-Tz, followed by purification of the mixtures and analysis of the labeled DNA on agarose gels (for details see the ESI†).

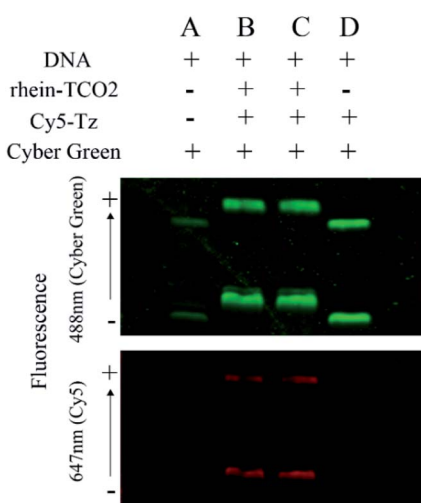


Fig. 7 Electrophoretic analysis of bioorthogonal chemistry reactions between pUC19 plasmid DNA (linearized by BamHI), **rhein-TCO2** and Cy5-Tz. DNA were all stained with cyber green, which is nucleic acid dye showing green fluorescence at 488 nm. The top gel shows cyber green fluorescence monitored at 488 nm, and the bottom gel is the same gel which showed Cy5 red fluorescence monitored at 647 nm. Reaction conditions for lane A: linearized pUC19 DNA were loaded with cyber green; reaction conditions for lanes B and C: linearized pUC19 DNA and **rhein-TCO2** were incubated for 12 h, and then reacted with Cy5-Tz for 30 min, and the mixture were loaded with cyber green after purified; reaction conditions for lane D: linearized pUC19 DNA and Cy5-Tz were incubated for 30 min without **rhein-TCO2**, and then the mixture were loaded with cyber green after purified.

A fluorescent image of the gel was shown in Fig. 7. DNA were stained with a green nucleic acid dye (cyber green, at 488 nm) for location on each lane and to distinguish the red fluorescence of Cy5 (at 647 nm). As illustrated in the gel at the top of Fig. 7, DNA presented two bands in each electrophoretic band (lane A–D), both of which were dyed green fluorescence. The lane A in the bottom gel shows that no red band was observed at the corresponding position of the green band when DNA was sampled separately in group A. Upon treatment with **rhein-TCO2** and Cy5-Tz, red fluorescence could be obviously observed at the same position of green fluorescence in each lane of lane B and lane C. We also investigated only DNA and Cy5-Tz were added in group D and observed that no red fluorescence was observed. Taken together, these results clearly indicated that the red fluorescence came from the combination of DNA and **rhein-TCO2**, and undergo biological orthogonal reaction with dye Cy5-Tz, which was consistent with that observed by laser confocal experiments in cell experiments.

We also evaluated the DNA binding ability of **rhein-TCO2**. The DNA binding ability K_{SV} value (Stern–Volmer quenching constant) for **rhein-TCO2** was $1.20 \times 10^4 \text{ M}^{-1}$, which was similar to that of rhein ($1.01 \times 10^4 \text{ M}^{-1}$) as reported in our previous studies.²³ In addition, we observed that **rhein-TCO2** could also be distributed into the nucleoli (mainly rRNA) of cells in laser confocal experiment. According to literature reports, anthraquinone compounds can not only bind to DNA, but also act as RNA embedders, such as antiviral compounds like amantantrone (HAQ) and mitoxantrone (DHAQ).²⁴ Therefore, we speculated that ribaric acid necrosis probes might have certain binding ability to RNA. The well-established UV-vis protocol was used to test the binding ability of RNA with rhein, and the K_{SV} value was $4 \times 10^3 \text{ M}^{-1}$, showing moderate binding ability (Fig. S2†).

Furthermore, to explain the observed results, the docking models were conducted to elucidate the possible binding mode of **rhein-TCO2** or rhein with DNA and RNA (Fig. 8 and S3†). As shown in Fig. 8B and S3A,† compound rhein and **rhein-TCO2** both had the same key interactions with DNA through interpolation. The compound **rhein-TCO2** with 6C alkyl chain spacer retained higher target affinity likely because of enough space for TCO group protruding out of the DNA groove. This may also be the reason why the modification of substituents at the 3 site of rhein-like necrosis probes does not affect the necrosis targeting

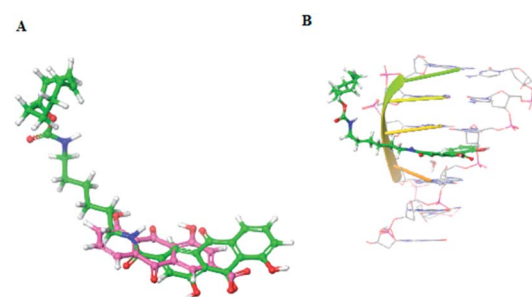


Fig. 8 (A) Chemical structure of rhein and **rhein-TCO2**; (B) predicted binding modes of **rhein-TCO2** with DNA (PDB code 282D).



of these molecules. Fig. S3B† showed the binding mode of rhein in RNA, rhein can be well embedded into the base pair plane of RNA single strand.

Conclusions

To conclude, we developed a biological orthogonal strategy to locate the distribution of rhein-like necrosis probes on necrotic cells and found that they were mainly distributed in the nucleus. And this copper-free method overcomes the limitation of the click-chemistry method of Cu(i) used in our previous study. Moreover, DNA electrophoresis and DNA binding ability experiments elucidated specific binding of the rhein-like necrosis probes to DNA in the nucleus and some rRNA in the nucleoli to achieve their necrosis targeting. In addition, molecular docking experiments also showed the binding events between rhein and DNA or rRNA through intercalation.

Conflicts of interest

There are no conflicts to declare.

Acknowledgements

We gratefully acknowledge the National Natural Science Foundation of China (No. 21907053 and 82003989), and we also thank the China Pharmaceutical University for providing spectra and Schrodinger Suites for molecular docking.

Notes and references

- 1 M. H. Wright and S. A. Sieber, *Nat. Prod. Rep.*, 2016, **33**, 681–708.
- 2 T. Böttcher, M. Pitscheider and S. A. Sieber, *Angew. Chem., Int. Ed.*, 2010, **49**, 2680–2698.
- 3 A. Rutkowska, D. W. Thomson, J. Vappiani, T. Werner, K. M. Mueller, L. Dittus, J. Krause, M. Muelbaier, G. Bergamini and M. Bantscheff, *ACS Chem. Biol.*, 2016, **11**, 2541–2550.
- 4 R. K. Amaravadi and C. B. Thompson, *Clin. Cancer Res.*, 2007, **13**, 7271–7279.
- 5 M. C. M. Stroet, E. de Blois, J. Haeck, Y. Seimbille, L. Mezzanotte, M. de Jong, C. W. G. M. Löwik and K. M. Panth, *Contrast Media Mol. Imaging*, 2021, **2021**, 2853522.
- 6 G. J. Kemerink, H. H. Boersma, P. W. Timister, L. Hofstra, I. H. Liem, M. T. Pakbiers, D. Janssen, C. P. Reutelingsperger and G. A. Heidendal, *Eur. J. Nucl. Med.*, 2001, **28**, 1373–1378.
- 7 Q. D. Nguyen, A. Challapalli, G. Smith, R. Fortt and E. O. Aboagye, Imaging apoptosis with positron emission tomography, *Eur. J. Cancer*, 2012, **48**, 432–440.
- 8 Y. Ni, G. Bormans, F. Chen, A. Verbruggen and G. Marchal, *Invest. Radiol.*, 2005, **40**, 526–535.
- 9 C. Wang, Q. Jin, S. Yang, D. Zhang, Q. Wang, J. Li, S. Song, Z. Sun, Y. Ni, J. Zhang and Z. Yin, *Mol. Pharmaceutics*, 2016, **13**, 180–189.
- 10 Q. Luo, Q. Jin, C. Su, D. Zhang, C. Jiang, A. F. Fish, Y. Feng, Y. Ni and J. Zhang, *Anal. Chem.*, 2017, **89**, 1260–1266.
- 11 Q. Wang, S. Yang, C. Jiang, J. Li, C. Wang, L. Chen, Q. Jin, S. Song, Y. Feng, Y. Ni, J. Zhang and Z. Yin, *Sci. Rep.*, 2016, **6**, 21341.
- 12 A. Zhang, T. Wu, L. Bian, P. Li, Q. Liu, D. Zhang, Q. Jin, J. Zhang, G. Huang and S. Song, *Mol. Imaging Biol.*, 2020, **22**, 515–525.
- 13 X. Zhang, B. Jin, W. Zheng, N. Zhang, X. Liu, T. Bing, Y. Wei, F. Wang and D. Shangguan, *Dyes Pigm.*, 2016, **132**, 405–411.
- 14 Q. Luo, Q. Jin, C. Su, D. Zhang, C. Jiang, A. F. Fish, Y. Feng, Y. Ni and J. Zhang, *Anal. Chem.*, 2017, **89**, 1260–1266.
- 15 Q. Jin, C. Jiang, M. Gao, D. Zhang, N. Yao, Y. Feng, T. Wu and J. Zhang, *New J. Chem.*, 2019, **43**, 6121–6125.
- 16 G. C. Rudolf and S. A. Sieber, *ChemBioChem*, 2013, **14**, 2447–2455.
- 17 M. Carmo-Fonseca, L. Mendes-Soares and I. Campos, *Nat. Cell Biol.*, 2000, **2**, E107–E112.
- 18 N. Perek, O. Sabido, N. Le Jeune, N. Prevot, J. M. Vergnon, A. Clotagatide and F. Dubois, *Eur. J. Nucl. Med. Mol. Imaging*, 2008, **35**, 1290–1298.
- 19 X. Duan, Z. Yin, C. Jiang, Q. Jin, D. Zhang, Z. Sun, W. Ye and J. Zhang, *Eur. J. Pharm. Biopharm.*, 2017, **117**, 151–159.
- 20 J. Kapuscinski, *Biotech. Histochem.*, 1995, **70**, 220–233.
- 21 A. A. Rybczynska, H. H. Boersma, S. de Jong, J. A. Gietema, W. Noordzij, R. A. J. O. Dierckx, P. H. Elsinga and A. van Waarde, *Med. Res. Rev.*, 2018, **38**, 1713–1768.
- 22 D. Zhang, M. Gao, Q. Jin, Y. Ni and J. Zhang, *Acta Pharm. Sin. B*, 2019, **9**, 455–468.
- 23 L. Bian, M. Gao, D. Zhang, A. Ji, C. Su, X. Duan, Q. Luo, D. Huang, Y. Feng, Y. Ni, Q. Jin and J. Zhang, *Anal. Chem.*, 2018, **90**, 13249–13256.
- 24 J. M. Jamison, K. Krabill, K. A. Allen, S. H. Stuart and C. C. Tsai, *Antiviral Chem. Chemother.*, 1990, **1**, 333–347.

